Laser & Photonics Reviews

LASER & PHOTONICS REVIEWS

www.lpr-journal.org

RESEARCH ARTICLE OPEN ACCESS

Laser-Based In Situ Diagnostics of Temperature and Material-Growth Dynamics in Photothermal Laser Nanoprinting of ZnO

Steven Kraus[1] | Kristian Kraft[2] | Yolita M. Eggeler[2] | Martin Wegener[1,3] | Paul Somers[1]

[1]Institute of Nanotechnology, Karlsruhe Institute of Technology, Karlsruhe, Germany | [2]Laboratory for Electron Microscopy, Karlsruhe Institute of Technology, Karlsruhe, Germany | [3]Institute of Applied Physics, Karlsruhe Institute of Technology, Karlsruhe, Germany

Correspondence: Paul Somers (paul.somers@kit.edu)

Received: 26 November 2025 | **Revised:** 24 March 2026 | **Accepted:** 30 March 2026

Keywords: optical in situ characterization | photothermal laser printing | zinc oxide

ABSTRACT

Photothermal laser printing using liquid inks has emerged as a facile alternative to multi-photon laser nanoprinting of semiconductor and metal structures. Applications lie, for example, in printed microelectronics. In previous experiments on ZnO, steady-state local temperatures in the laser spot, temperature dynamics, temperature profiles, and the dynamics of material growth have essentially been unknown. Herein, to determine these unknowns, we present in situ experiments using two co-focused lasers. A first continuous-wave laser at 405 nm wavelength heats a thin silicon film that serves as an absorber and thereby induces material deposition from a liquid ink. A second continuous-wave laser at 730 nm wavelength probes the local temperature via the calibrated temperature-dependent silicon-film optical transmission. The second laser also allows for monitoring the time-dependent laser-induced ZnO deposition via scattering of light. We find temperature increases of about 113 degrees Celsius at 1 mW laser power at 405 nm wavelength, with a fast component of the temperature change that rises and decays in the range of 1 µs. Furthermore, we find smooth material deposition beyond some ms timescales at low laser powers, whereas the transmission signal exhibits pronounced rapid temporal fluctuations at elevated laser powers.

1 | Introduction

3D laser printing of inorganic materials has recently found applications across many fields. The customizable nature of 3D additive manufacturing is particularly beneficial for rapid prototyping or changing requirements, such as is typical in scientific research. Compared to solely printing polymers, inorganic materials give access to a wider range of useful properties. Examples include the low mechanical damping and high optical transparency of glasses [1, 2], as well as the electrical conductivity of semiconductors [3–5] and metals [6, 7]. The generally increased chemical and temperature resistance also makes inorganics interesting for biological and chemical applications, such as implants [8] or microfluidics [9, 10].

The printing modalities of the various additive laser manufacturing techniques compatible with inorganic materials differ drastically [11, 12]. Inorganic materials can be printed via multi-photon processes, for example, by incorporation into polymers [13–16], photo-reduction-based resist systems [5, 17–21], agglomeration of nanoparticles [22], or nanoparticle sintering [23–25]. This allows the application of existing polymer printing techniques and therefore reuse of the very same equipment. It is also possible to laser print nanoparticles or arrange them in patterned structures by laser-generated micro-bubbles, a technique commonly known as bubble-assisted printing [26–28]. However, most structures printed using these techniques require postprocessing. In some cases, postprocessing can transform the as-printed structure dramatically and give it entirely new properties, such

as drastically reduced size [29, 30] or conversion into fused silica [31]. This conversion can even be done at temperatures well below conventional sintering temperatures. However, any post-treatment steps such as annealing, sintering, or etching may also impact structures in undesired ways, e.g., causing cracking [32]. In multi-material architectures, the different constituent materials may require different or even incompatible annealing or sintering conditions [13].

The technique we use in the present paper is photothermal laser printing [5, 28, 33–37]. Herein, material deposition is triggered by locally exceeding a certain temperature threshold. Sub-micrometer feature sizes and crystalline materials have been demonstrated [33]. Notably, photothermal printing does not require mode-locked laser sources. Low-power continuous-wave (cw) lasers have been shown to reach the required local temperatures [5]. The conditions during the photothermal printing process have, however, been essentially unknown. Material growth rate, crystallization, and morphology directly depend on the reaction kinetics, which are governed by temperature. Previous experiments on ZnO-based inks, for example, have surmised deposition temperatures in the range of 100°C–300°C [5, 33]. Prior characterization has been limited to post-printing analysis with indirect estimations of the temperature [34]. In contrast, the present paper focuses on in situ diagnostics. For the temperature measurements, we target sub-micrometer spatial resolution, sub-microsecond temporal resolution, and few-Kelvin temperature resolution. Optical "pump-probe"-type approaches appear well suited to meet these spatial and temperature resolution requirements [38–40]. Possible optical temperature-measurement approaches comprise reflectance-based measurements [41], Raman spectroscopy [42], and luminescence-based spectroscopy using upconversion nanoparticles [43, 44]. The latter two techniques require a spectrometer, complicating the optical setup. Adding nanoparticles is invasive and may affect the printing process. A desirable method is experimentally simple and provides a strong temperature-dependent signal.

Here, we use optical transmission measurements through a thin silicon film. Transmission provides a much larger temperature sensitivity than reflection in our system. The silicon film is already used as a local heat source by exciting it with a strongly focused "printing laser" operating at 405 nm wavelength. We add a second co-focused laser, the "probe laser," operating at 730 nm wavelength. After calibrating the temperature-dependent optical transmission of the probe laser through the silicon film, we derive the time-dependent and position-dependent temperature near the print zone at sub-microsecond temporal and sub-micrometer spatial resolution, respectively. Furthermore, we observe the printing of ZnO in situ at 100 µs resolution using the same setup and correlate the findings with our previous work [33].

2 | Results and Discussion

2.1 | Experimental Setup

Figure 1a shows a schematic of the experimental setup. A 405 nm wavelength cw laser, henceforth called the "printing laser," enters through a microscope objective lens, a glass coverslip, and the ink reservoir to finally be focused onto a silicon (Si) film. On top of this sputtered 300 nm thick amorphous silicon film, there is a sputtered 15 nm silicon dioxide layer to provide electrical insulation for future device applications. A part of the optical energy is absorbed and heats the nearby ink, inducing material deposition. The 405 nm wavelength is chosen to enable a small diffraction-limited focal spot while the light is not significantly absorbed by the ink itself [33]. As a response to the heating, the silicon film also changes its optical transmission (and reflection) of the probe laser at 730 nm wavelength [45]. This wavelength choice results from a trade-off: On the one hand, to minimize heating by the probe laser while maintaining a certain signal strength on the detector, long wavelengths corresponding to large transmission of the silicon film are favored. On the other hand, the relative transmission change vs. temperature increases for shorter visible wavelengths. For both lasers, we choose readily available, low-cost, cw lasers.

We start our experiments by using pure dimethyl sulfoxide (DMSO) instead of the ink, which is primarily composed of DMSO. This is to avoid material depositing during the initial temperature measurements. A detector behind the sample collects a fraction of the light transmitted at 730 nm wavelength (the silicon film is essentially opaque to the printing laser). The detector therefore generally measures both the transmission of the silicon film and changes in optical forward-scattering.

Figure 1b,c shows numerical calculations of the temperature profile around the heated regions, 1 µs and 25 ms after switching on the printing laser, respectively. The greyscale indicates the local temperature increase $\Delta T = T\text{-}T_0$ with respect to the ambient temperature ($T_0 = 294.15$ K). The temperature profile is highly localized, both parallel and normal to the substrate. This localization arises from the combination of a small heating source, in this case a nearly diffraction-limited laser focus, a high absorption inside the silicon film, and a relatively low thermal conductivity of the surrounding environment, thereby enabling sub-micrometer printing of ZnO [33]. In the calculations, losses in incident laser power on the way to the substrate are also allowed as a degree of freedom for calibrating numerical parameters to experimental conditions (see Figure S1). This is due to the fact that experimentally, the laser power is measured before the objective lens and not directly at the sample. After this calibration to the experimental data, the numerical calculations quantitatively represent the conditions and results of the experiments.

2.2 | In Situ Temperature Measurements Using DMSO

First, the power of the probe-laser transmitted through the silicon film and arriving on a detector, $S(\Delta T)$, is measured as a function of the temperature change with respect to ambient temperature, ΔT. This is done by mounting the silicon-coated substrate on a temperature-controlled heating stage. Corresponding data $S(\Delta T)/S(\Delta T = 0)$ and methodology are available in Figure S2. These measurements are nicely fitted by the formula in Equation (1),

$$\frac{S(\Delta T)}{S(\Delta T = 0)} = exp\left(\frac{-4\pi d}{\lambda} k_T \cdot \Delta T\right) \quad (1)$$

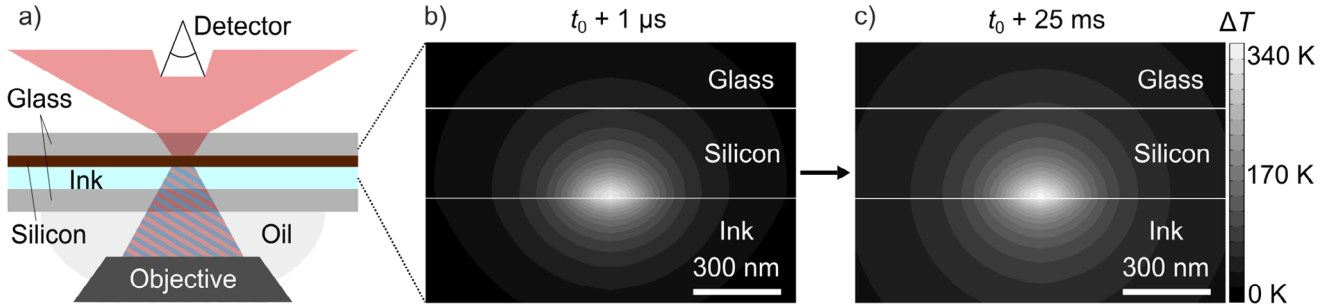

FIGURE 1 | Schematic of laser printing chamber and numerical calculations of temperature profiles. (a) Schematic of the optical setup allowing for photothermal laser printing with integrated in situ laser diagnostics. A tightly focused first continuous-wave ("printing") laser at 405 nm wavelength locally heats the sample by absorption of light in a thin Si/SiO_2 film and thereby induces dissociation of precursor molecules in solution (the "ink") and thus material deposition onto that substrate. A fast photodiode monitors the temperature-dependent transmission of a co-focused second cw ("probe") laser at 730 nm wavelength through the film. The detector is intentionally placed not to detect the entire solid angle of transmitted light of the probe laser, such that the detector signal becomes susceptible to changes in the forward scattering of light arising from material being deposited. (b) Numerical calculation of the temperature profile 1 µs after start of 1 mW printing laser exposure, and (c) after 25 ms. The relative detector signal, which is defined by the ratio of the detector signal at time t_0 divided by the average of the detector signal at negative times, i.e., before the printing laser has been switched on, is recorded. The relative detector signal can thereby exceed unity.

where d is the silicon film thickness, λ is the free-space probe laser wavelength, and k_T is the linear coefficient with which the imaginary part of the refractive index changes. It is straightforward to derive this formula from the usual Fabry–Perot equation under the assumption that the reflectances are nearly temperature independent, the film is strongly absorbing, and that the absorption coefficient changes linearly with temperature in the spirit of a Taylor expansion. We obtain a fit of the formula to the calibration experiment for $k_T = 3.73 \times 10^{-4}$ K^{-1}. The good fit indicates that this interpretation of the signal temperature dependence is correct. However, we note that this fitting process is not necessarily required to calibrate the temperature response in the experiment.

Next, the silicon film transmission is measured in situ as a function of the printing laser power and averaged over 10 measurements (Figure 2a, left-hand side vertical scale). Here, the detector has a viewing angle of 32°. Using the aforementioned calibration, we have converted these data to temperature as a function of printing laser power (Figure 2a, right-hand side vertical scale). The probe laser is turned on some time before t_0, modulated at 50 kHz frequency and 50% duty cycle with 60 µW peak power. The heating due to this probe laser power is calculated to raise the silicon film temperature by an average of 3 K. A silicon photodetector captures most of the transmitted light, and the resulting signal is processed using a lock-in amplifier. At time t_0, the printing laser is turned on and slowly ramped from printing power $P_0 = 0$ mW to 2 mW in 0.02 mW steps. A 5 ms pause is introduced between each power step to allow the temperatures to reach a respective steady state. The experimental data are well fit with Equation (1), which again supports our description of the temperature-dependent transmission. Data is only shown up to $P_0 = 1$ mW due to the formation of micro-bubbles at higher printing laser powers, which disturb the measurement. To determine the rate of temperature increase with printing laser power, C, we assume a linear relationship of $\Delta T = C \times P_0$, where ΔT is independent of exposure time by the printing laser. This relationship is justifiable with the assumptions that there is negligible change in reflection of the printing laser within the observed temperature range, and that the non-reflected part of the printing laser is completely absorbed. The data in Figure 2a reveals $C = 113 \pm 0.62$ K mW^{-1}.

The optical transmission through the silicon film does not indicate the peak temperature within the printing region, but rather an average temperature. This is due to the fact that the focal spot of the longer-wavelength probe laser is larger than that of the printing laser. The transmission depends on the accumulated absorption throughout and across the entire temperature profile. Therefore, all experimentally determined temperatures in this work are reported as average temperatures. To analyze the spatial distribution of the temperature field caused by heating from the printing laser, we use the same setup but simply displace the printing laser focus in discrete increments relative to the probe laser. Displacing it in steps of 20 nm, as measured at the sample, allows high spatial resolution measurements of the temperature profile. In Figure 2b, the measured temperature profiles scanned along one axis are shown. Each point in the plot shows the temperature increase ΔT as measured when the two laser foci are displaced by the print-probe displacement Δx. The measured temperature profiles are symmetric and increase proportionally to printing laser power. They have a full-width half-maximum (FWHM) of roughly 740 nm, which supports the few-hundred-nm printing line widths observed in previous work [33]. Underneath the temperature profiles in the figure, the point spread functions of the printing laser and the probe laser foci are shown to scale (also found in Figure S3). These show that the probe laser is larger than the printing laser focus and also possesses a prominent diffraction ring. Both of these factors, as well as the variation of the temperature increase inside the silicon film, contribute to a broadening of the temperature profile in the measurement. We account for the dependence of the probe laser transmission on the spatial temperature profile in the numerical calculations shown in Figure 1. Through these calculations, we estimate that the real FWHM of the (unconvoluted) spatial temperature profile is 320 nm. Using a thermally driven chemical reaction, a sharp reaction threshold in the Boltzmann distribution has enabled us to print ZnO material

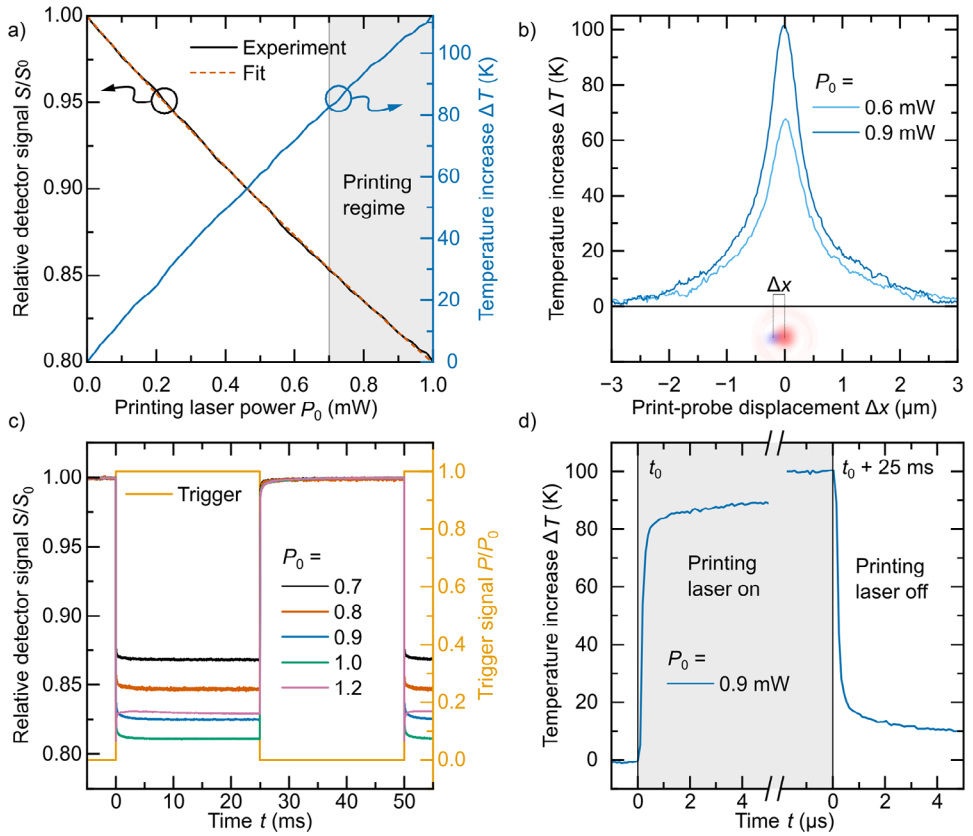

FIGURE 2 | In situ measurements using dimethyl sulfoxide (DMSO) as the ink. The printing laser is switched on at time t_0, and the detector records the signal S relative to $S_0 = S(t < t_0)$, which corresponds to the transmitted probe laser light. (a) The recorded relative detector signal of the co-focused probe laser vs. printing laser power P_0 under stationary conditions (left vertical scale), where P denotes the time-dependent printing laser power. On the right vertical scale, this signal is converted into a temperature increase ΔT with respect to room temperature. The conversion becomes possible with the help of a calibration experiment (see Figure S2). The printing regime indicates laser powers at which ZnO lines can be printed. (b) Spatial temperature profiles recorded by displacing the printing laser focus with respect to the probe laser focus under stationary conditions. Δx is the center-to-center distance between the probe and printing laser foci. The to-scale measured point spread functions of both the printing and probe lasers are depicted. (c) Averaged time-dependent measurements of the probe laser transmission through the silicon film for various printing laser powers, acquired with a faster silicon avalanche photodetector than used in previous panels. The laser-on signal of the printing laser, as measured by another fast photodetector, is plotted as the Trigger signal for reference. (d) Zoomed in view of the signal measured at 0.9 mW printing laser power from panel (c). The relative detector signal for both the beginning and end of the printing laser on-time is shown.

with feature sizes on the order of 300 nm or less (see [33] and below).

Figure 2c shows the time dynamics before reaching steady-state conditions of sample heating for various printing laser powers P_0. The measurements are conducted with the probe laser unmodulated at 60 μW average power and the printing laser modulated at 20 Hz frequency with 50% duty cycle. To capture the transmitted probe laser light, the silicon photodetector from previous experiments is swapped out for a smaller-area silicon avalanche photodetector with a higher bandwidth of 10 MHz. The bandwidth is necessary to accurately measure the temporal dynamics of the heating. However, a significantly smaller portion of transmitted light is captured through a 2.9° viewing angle by this detector. Due to temperature-dependent changes in forward-scattering, such as a microlensing effect, this leads to relative detector signals different from Figure 2a. Temperature conversion of the signal from the new detector is instead achieved via the known temperature response to printing laser power. The printing laser is turned on and off 10 000 times at each power, and the detector signal is averaged directly on an oscilloscope to improve the signal-to-noise ratio. The relative detector signal reaches a steady state after a few milliseconds, indicating that the temperature is stable. Noticeably, for $P_0 = 1.2$ mW the signal drops immediately after t_0 due to the heated absorption of the silicon film, but then rapidly increases to a level above that of the $P_0 = 1$ mW curve. This behavior might be due to the formation of microbubbles, which can be observed to start forming at similar printing laser powers. However, it is challenging to determine the exact cause. Figure 2d shows a zoomed-in plot of the $P_0 = 0.9$ mW data from Figure 2c, revealing that a temperature value 70% of the steady state is reached within 300 ns after the start of laser exposure at $t = t_0$. Similarly, the temperature approaches ambient temperature very quickly after the end of printing laser exposure at $t = t_0 + 25$ ms. This fast heating and cooling is reasonably expected due to thermal conduction on this microscopic scale and can be reproduced by numerical calculations (Figure S1).

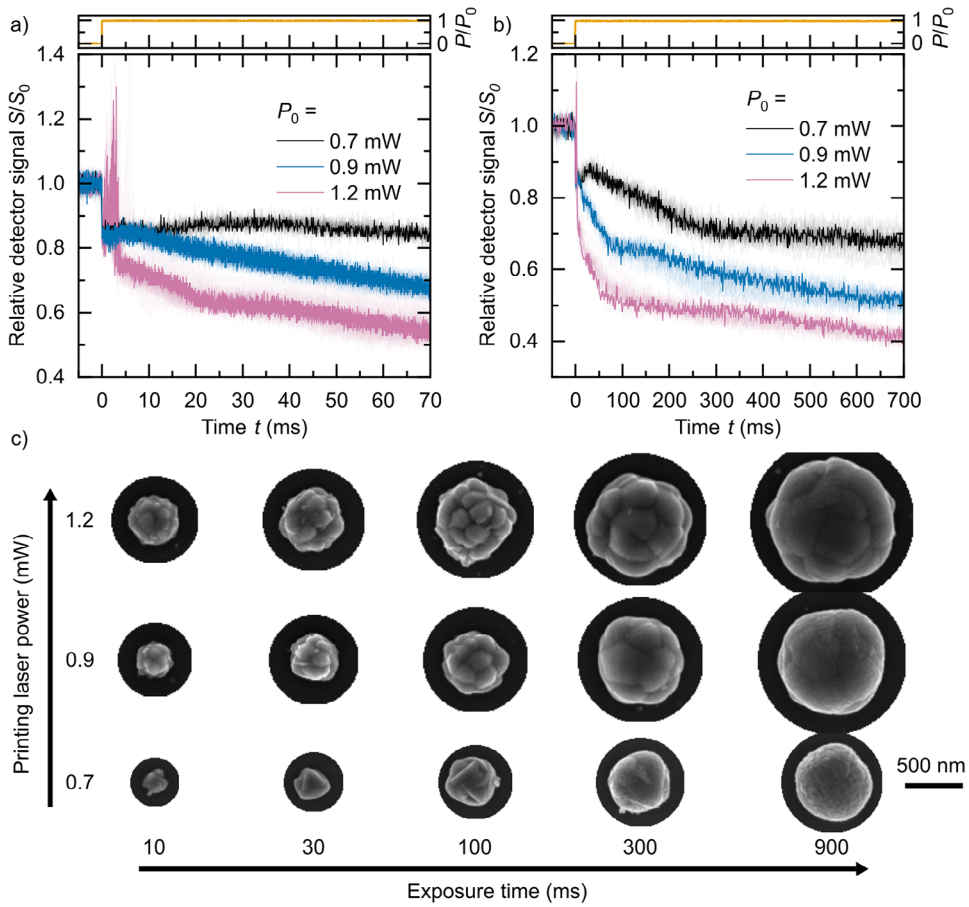

FIGURE 3 | Time-dependent measurements and SEM images of ZnO structures under stationary printing laser exposures. (a) First few milliseconds of relative detector signal during ZnO deposition. (b) Longer timescale view of the signals from panel (a). Individual traces are overlaid for 20 separate exposures (pale curves) to illustrate repeatability. Selected individual experiments are highlighted by color. (c) Selected SEM images of ZnO growth resulting from stationary point exposures for varying printing laser powers and different exposure times.

2.3 | Dynamics of ZnO Deposition Under Stationary Conditions

Next, similar experiments are carried out using a ZnO ink composed of zinc formate in DMSO. Now, the relative detector signals are also sensitive to scattering off material deposition during printing laser exposures, alongside the temperature-dependent substrate transmission. Changes in the relative detector signal beyond the initial drop shown in Figure 2c,d now indicate deposition of material. Additionally, measurements cannot be easily repeated under the exact same conditions due to the permanent material depositions. As such, the measurements are subject to more statistical noise and slightly changing dynamics for each exposure.

In Figure 3a, the printing laser exposes a single stationary point for several hundred milliseconds while monitoring the probe laser transmission. The initial drop in transmission of the probe laser on the detector corresponds to the results obtained above using solely DMSO. A close-up of this can be found in Figure S4. Due to the temperature-dependent transmission, the traces for higher printing laser powers show ultimately lower relative detector signals. For the tested laser powers, deposition of ZnO appears to occur on the millisecond timescale, shown by a rising section of the signal after the initial drop. For example, in the oscilloscope trace for $P_0 = 0.7$ mW printing laser power, this rising signal then peaks at 30 ms. This is the lowest printing laser power for which material deposition can be observed after a one second exposure. Referencing Figure 2a, a printing laser power of 0.7 mW corresponds to an average temperature increase at the sample of $\Delta T = 79 \pm 0.45$ K + $(3 \pm 0.017$ K$) = 82 \pm 0.47$ K. This implies a ZnO deposition average temperature of 376.2 ± 0.47 K, or 103 ± 0.47°C under the given experimental conditions. While slightly lower printing laser powers may still result in material deposition on yet longer exposure timescales, only small further reductions in deposition temperature should be expected due to the exponential dependence in the Boltzmann distribution. For higher laser powers, the aforementioned peak shifts to earlier times, indicating a higher rate of measurable material growth. At $P_0 = 0.9$ mW, this peak can be found at $t = 5$ ms. At higher printing laser powers, strong fluctuations in the relative detector signal near the bandwidth limit of the detector are observed immediately after turning on the printing laser. This can be seen in the trace for $P_0 = 1.2$ mW printing laser power. The cause of these disturbances is unknown. However, we recall that in plain DMSO, this printing laser power causes bubbles to form. Therefore, it is likely these fluctuations stem from either microbubbles or uncontrolled material growth. Notably, Figure 1 implies local temperatures can reach well above the boiling point of DMSO even for printing laser powers near the threshold, yet

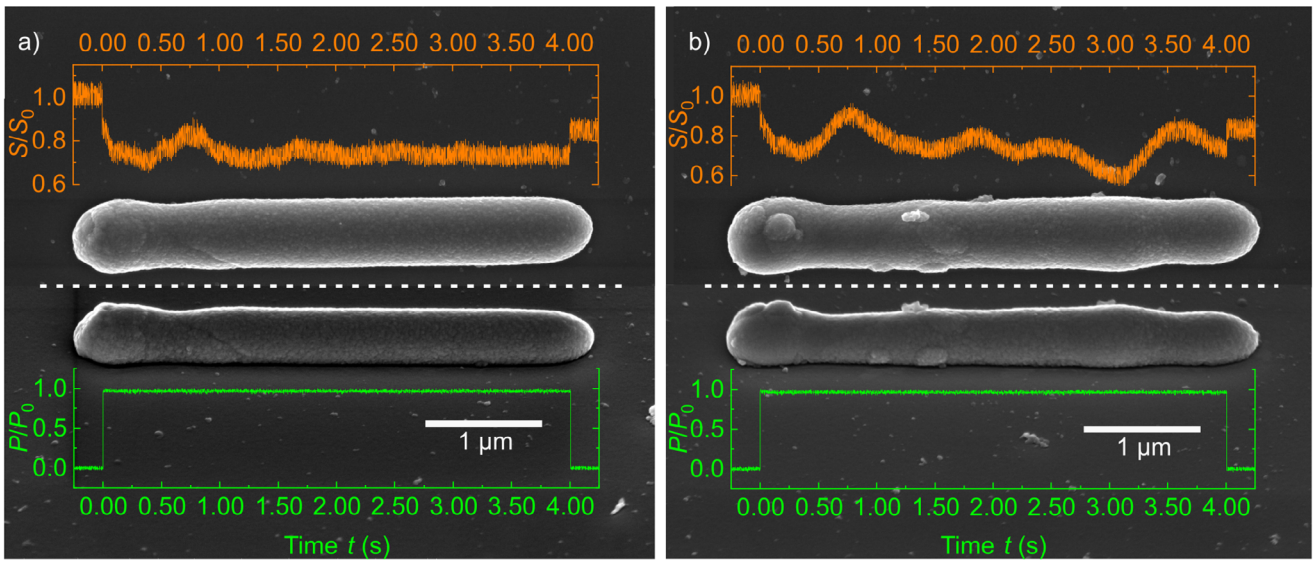

FIGURE 4 | Two printed ZnO lines (under nominally identical conditions) with co-focused printing and probe laser. The foci are scanned from left to right with respect to the sample at a constant velocity of 1 µm s^{-1}, with printing laser power at $P_0 = 0.8$ mW. The panel centers show top-view (top) and oblique-view (bottom, 52° angle with respect to the surface normal) scanning electron micrographs of the same line, respectively, to give an impression of the width and height of the lines. The in situ transmission signals (orange curves) and the time traces of the print laser power (green curves) are overlaid. Note that the time scales here are much longer than those shown in Figure 3. (a) Example of a printed ZnO line. (b) Same conditions as in (a), but the line exhibits larger variations in width and height.

surface tension effects likely prevent measurable microbubble formation under these conditions [46–48]. Thus, for well-defined, controllable, and micro-scale ZnO formation, we deem printing laser powers above 1 mW unsuitable.

Looking at longer timescales of the same data, Figure 3b shows that the continued growth of ZnO leads to further decreasing relative detector signals. Changes in the slope of the signal can also be spotted in regular intervals. We propose that this is due to thin-film interference inside the ZnO structure, modulating the transmission as it grows. These changes in slope occur at earlier times for higher printing laser powers, indicating faster material growth, in line with logarithmic growth of hydrothermally deposited ZnO found in previous work.

Figure 3c shows scanning electron microscopy (SEM) images of ZnO structures obtained by exposing stationary points to different printing laser powers for varying exposure times. At the printing threshold, laser power $P_0 = 0.7$ mW, the first structures observable after sample development are found for exposures of 10 ms. With increasing printing laser power and exposure time, the size of the structures clearly increases. Previous work has shown that the ZnO structures exhibit polycrystallinity with random grain orientation [33]. However, the random grain orientations likely do not contribute to the repeatable slope changes observed in Figure 3b. The end of material growth occurs on a timescale similar to the cooling time of the sample temperature, as shown in Figure S4.

2.4 | Dynamics of ZnO Deposition Under Scanning Conditions

Through scanning the substrate relative to the two co-focused laser foci, lines of ZnO are formed, and the in situ transmission signal of the probe laser is collected. First, the probe laser is turned on while the substrate is moving at a scan velocity of 1 µm s^{-1}. At $t = t_0 = 0$, the printing laser is switched on at a power of $P_0 = 0.8$ mW. After 4 s, the printing laser is switched off and scanning stops. The relative detector signal varies during printing as shown by the time traces (orange curves) in Figure 4a,b. The two experiments are performed under nominally identical conditions, yet the results are different, demonstrating by example that the in situ signal does provide valuable information. Given the known scan velocity, the time axis is connected to the real-space position in the SEM images except for an unknown offset or shift. In Figure 4a,b, we have ad hoc chosen this offset such that the print time intervals (green curves) and the SEM images are horizontally centered with respect to each other. Despite this offset ambiguity, the comparison of in situ signals and SEM images allows us to derive relevant signal-morphology correlations. In Figure 4a, the right half of the SEM image shows a rather smooth line, and the in situ signal is rather flat. By comparison, the right half of the SEM image in Figure 4b shows a rough line and the in situ signal exhibits notable fluctuations in height and width. The left half of the SEM images both show a thicker line at the beginning, followed by a constriction. The corresponding time traces reveal a variation of the in situ signal on the same scale. A collection of relative detector signals from all line experiments is shown in Movie S1. Oblique-view SEM imaging revealed that the varying relative detector signal also correlates with variation in the ZnO line height. Combined, we conclude that temporal variations of the in situ signal correlate with thickness variations of the printed lines. It is presently unclear what causes these variations in line width during printing. Here, we print single-crystalline ZnO lines, as confirmed by electron backscatter diffraction (EBSD) analysis shown in Figure S5. It has been observed previously that the line width variations sometimes also occur in both single-crystalline and polycrystalline lines [33]. We therefore speculate

that the variations might stem from inhomogeneities of the ink or small unwanted mechanical vibrations in the setup. When printing the lines at a ten times larger scan velocity of 10 μm s^{-1}, we have observed no variations in the in situ relative detector signal during printing within the noise at all—despite material being formed as evidenced by SEM imaging (not depicted). We interpret these findings in that the ZnO material growth front lags behind the instantaneous position of the two co-focused lasers.

3 | Conclusions

In this work, we explored the temperature dynamics behind the photothermal laser printing of ZnO. The presented methodology made use of the temperature-dependent transmission of the substrate to non-invasively characterize the printing process in situ. We determined a locally averaged temperature increase of ∼113 K per mW of printing laser power, where the heating and cooling occur over very short time scales, on the order of 300 ns. The developed spatial temperature profiles are strongly localized within ∼300 nm lateral dimension, enabling laser printing of sub-micrometer ZnO structures. The sensitivity of the in situ measurement to light scattered off printed material shows strong potential as a diagnostic tool for print quality and uniformity. Additionally, it provides information about the material growth rate, such that ZnO growth begins within 10 ms of substrate heating. Our findings here provide guidance for the future development of photothermal laser printing technologies, including precursor selection for inks beyond ZnO (i.e., metals or insulating oxides). Further, these insights into the photothermal heating process will provide a strong foundation for approaching the variable temperature dynamics in more complex environments (i.e., multi-material printing [49] or other substrates [50, 51]). Ultimately, through a well-controlled heating process, photothermal laser printing provides a promising route to low-cost, multi-material microelectronic device fabrication.

4 | Experimental Methods

4.1 | Substrate Preparation

Borosilicate glass coverslips (Marienfeld, No. 1.5H, 22 × 22 × 0.17 mm) were used to make the substrates. To remove surface contaminants, the coverslips were sonicated at 60°C for 10 min each in aqueous solutions of 4 vol-% Deconex OP 146, 2 vol-% Deconex OP 12PA-x, and 2 vol-% Deconex OP 171, in that order. Each step was followed by sonication in ultrapure water under identical conditions. The substrates were then dried under a nitrogen stream.

The absorbing silicon layer was deposited by magnetron sputtering (BOC Edwards Auto 500) at a power of 200 W with an argon flow rate of 3.5 sccm. After this first deposition, the process gas was switched to ambient air to sputter an additional 15 nm silicon dioxide film under otherwise similar conditions. Finally, the printing substrates are annealed at 250°C for 3 h. This annealing step prevents permanent change of the film properties during the measurements.

For printing, the substrates were assembled with the ink sandwiched between the sputtered surface and a glass coverslip. A single layer of Kapton tape (≈ 61 μm thick) served as a spacer to define the ink reservoir. A detailed schematic of the printing cell and detector geometry can be found in Figure S6. After printing, the samples were developed sequentially in 20 mL baths of DMSO (10 min) and isopropanol (2 × 10 min) and then dried by a stream of nitrogen.

4.2 | Ink Formulation

The zinc formate ink was prepared by dispersing 500 mg (3.22 mmol) of $Zn(HCO_2)_2$ in 10 mL of dry DMSO inside a 20 mL crimp-cap vial with 4 Å molecular sieve. The suspension was sonicated for 15 min and then agitated for 4 h at 30°C and 400 rpm on an orbital shaker to ensure homogenization. It was subsequently left undisturbed for 12 h at room temperature to allow coarse particles to sediment. It was then filtered with a 0.20 μm hydrophobic PTFE syringe filter (Ø 25 mm, VWR) into a crimp-cap vial. The resulting ink was stored under nitrogen until use.

4.3 | Optical Setup

Printing and in situ probing were performed on a custom-built laser microprinting system. A sample holder allowing light transmission was mounted on an Aerotech ANT130XY-160 and ANT130LZ-060 stage combination, driven by one iXC2e and two XC2e controllers.

A 405 nm wavelength printing laser (Toptica iBEAM SMART 405-S) and a 730 nm wavelength probe laser (LP730-SF15 driven by CLD1010LP) were co-focused onto the sample using a Zeiss Apochromat 100× 1.4 NA oil-immersion objective. The position of the printing laser on the sample was controlled by a Newport Picomotor 8742 connected to a Newport 8821 motorized mirror mount holding a mirror. The two laser beams passed through the immersion oil, the uncoated top coverslip, and approximately 60 μm of ink before reaching the silicon dioxide/silicon layer. Laser powers, P_0, were defined as the optical power transmitted through a 5.3 mm diameter circular aperture placed at the objective back focal plane. This power can routinely be measured, whereas the power in the focal region of an immersion-oil system cannot. Unfortunately, further internal apertures of the objective lens influence the power in the focal region. Therefore, we here used numerical calculations to calibrate the ratio of the power in the focus inside the silicon film and that passing through the 5.3 mm diameter aperture. We found this ratio to be 17.7%. On this basis, we determined the following power densities for the 405 nm laser: 1.7×10^5 W cm^{-2} ($P_0 = 0.7$ mW), 2.0×10^5 W cm^{-2} ($P_0 = 0.8$ mW), 2.2×10^5 W cm^{-2} ($P_0 = 0.9$ mW), 2.5×10^5 W cm^{-2} ($P_0 = 1$ mW), and 3.0×10^5 W cm^{-2} ($P_0 = 1.2$ mW). Likewise, the intensity of the 730 nm wavelength laser was estimated to be 1.5×10^4 W cm^{-2} for 60 μW measured through the same 5.3 mm diameter aperture. The two beam paths were combined via a Thorlabs MH254H45 hot mirror before entering the objective lens. Power adjustments were made for each beam using a half-wave plate (WPH10ME-405 for the printing laser, WPH10ME-780 for the probe laser) and a polarizing beam splitter (Thorlabs PBS252 for the printing laser, PBS251 for the probe). Quarter-

wave plates (WPQ05ME-405 for the printing laser, EKSMA Optics 467–4410 achromatic quarter-wave plate for the probe laser) were used to circularly polarize the beams. Both lasers were expanded to significantly overfill the objective. The printing laser was strongly absorbed by the silicon film, whereas the probe laser was transmitted and detected behind the sample using either a silicon photodetector (Thorlabs FDS1010) for the time-averaged measurements in Figure 2a,b, or an avalanche photodetector (Thorlabs APD410A/M) for all the others, with the active surface positioned 5 mm or 10 mm above the sample, respectively. During the experiments, the illumination light and room lights were turned off. The position of the printing interface was determined using an astigmatic reflective detection scheme [52]. The reflected part of the probe laser was recollected by the objective lens, separated by the polarizing beam splitter, and then passed through two cylindrical lenses (f = 75 mm and 150 mm, placed 70 mm and 190 mm from the detector) before reaching a four-quadrant photodetector (S4349 four-quadrant photodiode in custom-built housing).

The sample was illuminated in reflection mode by a 660 nm LED (Thorlabs M660FP1), coupled into the objective via a 450 nm dichroic mirror (Edmund Optics 69–887), and observed using a color USB camera (BFS-U3-50S4C-C). The analog signals from the quadrant photodetector and the silicon avalanche photodetector were recorded via one XC2e controller each, while the silicon photodetector output was first processed using a lock-in amplifier (SR844) before being recorded by the iXC2e. Some experiments were recorded using an oscilloscope (Sigilent SDS5034X).

4.4 | Transmission Measurements

Co-alignment of the two laser beams was performed in situ. The probe beam was first centered in the camera field of view and its power set to 60 μW. The printing laser was then modulated at 50 kHz frequency and spatially moved across the probe laser focus while monitoring the modulation depth of the transmission recorded by the silicon photodetector. Alignment was refined iteratively in all three axes until the modulation amplitude was maximized.

For steady-state measurements (Figure 2a,b), the probe laser was modulated at 50 kHz and processed using a lock-in amplifier. The printing laser was operated in a steady state. For time-resolved experiments (Figure 2c,d), the probe laser was not modulated, and its signal was recorded directly and averaged over 10 000 periods of the printing laser modulated at 20 Hz frequency. The oscilloscope sampling rate and detector bandwidth were 10 MSa s^{-1} and 10 MHz, respectively.

4.5 | Calibration Experiment

To calibrate the temperature-dependent transmission of the silicon film, the previously manufactured sample was placed on an HCS302 temperature-controlled stage, controlled by an Instec MK2000 precision temperature controller. It is mounted by a 60 μm thick piece of Kapton tape, before putting on a droplet of DMSO and covering it with a ground glass diffuser to suppress interference from the glass coverslip on which the silicon film has been sputtered. The probe laser is set to a power of 60 μW, focused by a 500 mm focal length lens and modulated at 50 kHz frequency with 50% duty cycle. A silicon photodetector (Thorlabs FDS1010) placed behind the stage collects the transmitted light of the probe laser, after which it is processed by a lock-in amplifier to read out the signal. The measurement starts at ambient temperature, then increases the temperature by steps of 3°C until reaching 200°C. Heating between each step takes roughly 1 min, after which an additional pause of 20 s allows the temperature to stabilize before measuring the detector signal. At around 100°C, the DMSO starts evaporating. To prevent the interface from drying up, the DMSO was therefore manually refilled in regular intervals using a pipette. We use Gaussian error propagation from the fitted calibration curves in Figure S2 to determine the final uncertainty in our in situ temperature measurements.

4.6 | Scanning Electron Microscopy

The scanning electron microscope (SEM) imaging of the ZnO structures was carried out in a Thermo Scientific Helios G4 FX DualBeam System. ZnO point exposures printed at 0.9 and 1.2 mW and ZnO lines printed at 0.8 mW were acquired at an acceleration voltage of 5 kV, a working distance of 4 mm, and a nominal beam current of 0.4 nA. The SEM images in the supporting information were acquired with the same settings. SEM images of the point exposures printed at 0.7 mW were acquired at 3 kV and a nominal beam current of 0.8 nA. The sample was coated with an approximately 10 nm thick carbon layer before imaging.

4.7 | Electron Backscatter Diffraction

EBSD was performed in a Thermo Scientific Helios G4 FX combined focused ion beam (FIB) and SEM dual beam system. The printed ZnO line was first prepared by FIB milling to achieve a flat-top ZnO surface. The sample was mounted on a 45° pretilted sample holder, then tilted in the SEM until the sample surface and FIB pole piece were aligned at a relative angle of 0.3° [33]. For milling, an ion beam acceleration voltage of 30 keV and a nominal current of 26 pA was used. After sample preparation, the sample was mounted on a 70° pre-tilted holder, and EBSD patterns were acquired at 20 keV acceleration voltage and nominal current of 6.4 nA. The acquisition of the pattern and subsequent data processing were done with the Bruker Esprit 2.3 software. A Hough transformation was used for Kikuchi pattern indexing, and subsequent orientation analysis was performed using the MTEX toolbox (version 5.10.2) [53] for MATLAB.

Acknowledgements

We acknowledge funding by the Deutsche Forschungsgemeinschaft (DFG, German Research Foundation) under Germany's Excellence Strategy for the Excellence Cluster "3D Matter Made to Order" (2082/1–390761711; 2082/2–390761711), by the Carl Zeiss Foundation, and by the Helmholtz program "Materials Systems Engineering".

Open access funding enabled and organized by Projekt DEAL.

Conflicts of Interest

The authors declare no conflicts of interest.

Data Availability Statement

The COMSOL files and python scripts are available in the open-access data repository of Karlsruhe Institute of Technology (https://doi.org/10.35097/1ede29pa9yww96ms). Other data that support the findings of this study are available from the corresponding author upon reasonable request.

References

1. Z. Li, Y. Jia, R. Xiao, et al., "3D-Printed Fused Silica Glass Microlattice as Mechanical Metamaterial," *Cell Reports Physical Science* 5 (2024): 102172, https://doi.org/10.1016/j.xcrp.2024.102172.

2. J. Köpfler, T. Frenzel, J. Schmalian, et al., "Fused-Silica 3D Chiral Metamaterials via Helium-Assisted Microcasting Supporting Topologically Protected Twist Edge Resonances with High Mechanical Quality Factors," *Advanced Materials* 33, no. 40 (2021): 2103205, https://doi.org/10.1002/adma.202103205.

3. G. Liu, Z. Ma, G. Li, et al., "All-Printed 3D Solid-State Rechargeable Zinc-Air Microbatteries," *ACS Applied Materials & Interfaces* 15, no. 10 (2023): 13073–13085, https://doi.org/10.1021/acsami.2c22233.

4. Y. Han, J. Guo, Q. Luo, and C.-Q. Ma, "Solution-Processable Zinc Oxide for Printed Photovoltaics: Progress, Challenges, and Prospect," *Advanced Energy and Sustainability Research* 4, no. 10 (2023): 2200179, https://doi.org/10.1002/aesr.202200179.

5. L. Yang, H. Hu, A. Scholz, et al., "Laser Printed Microelectronics," *Nature Communications* 14, no. 1 (2023): 1103, https://doi.org/10.1038/s41467-023-36722-7.

6. S. Bagheri, K. Weber, T. Gissibl, T. Weiss, F. Neubrech, and H. Giessen, "Fabrication of Square-Centimeter Plasmonic Nanoantenna Arrays by Femtosecond Direct Laser Writing Lithography: Effects of Collective Excitations on SEIRA Enhancement," *ACS Photonics* 2 (2015): 779–786, https://doi.org/10.1021/acsphotonics.5b00141.

7. D. Pavlov, S. Syubaev, A. Kuchmizhak, et al., "Direct Laser Printing of Tunable IR Resonant Nanoantenna Arrays," *Applied Surface Science* 469 (2019): 514–520, https://doi.org/10.1016/j.apsusc.2018.11.069.

8. F. Yang, C. Chen, Q. Zhou, et al., "Laser Beam Melting 3D Printing of Ti6Al4V Based Porous Structured Dental Implants: Fabrication, Biocompatibility Analysis and Photoelastic Study," *Scientific Reports* 7, no. 1 (2017): 45360, https://doi.org/10.1038/srep45360.

9. A. Zhang, J. Xu, Y. Li, et al., "Three-Dimensional Large-Scale Fused Silica Microfluidic Chips Enabled by Hybrid Laser Microfabrication for Continuous-Flow UV Photochemical Synthesis," *Micromachines* 13, no. 4 (2022): 543, https://doi.org/10.3390/mi13040543.

10. R. Su, F. Wang, and C. McAlpine, "3D printed Microfluidics: Advances in Strategies, Integration, and Applications," *Lab on a Chip* 23 (2023): 1279–1299, https://doi.org/10.1039/D2LC01177H.

11. S.-F. Liu, Z.-W. Hou, L. Lin, Z. Li, and H.-B. Sun, "3D Laser Nanoprinting of Functional Materials (Adv. Funct. Mater. 39/2023)," *Advanced Functional Materials* 33, no. 39 (2023): 2211280, https://doi.org/10.1002/adfm.202211280.

12. P. Bian, Z.-Y. Hu, X.-Q. Liu, et al., "Laser Printing High-Resolution Inorganic 3D Microstructures," *Laser & Photonics Reviews* (2025): 01797, https://doi.org/10.1002/lpor.202501797.

13. J. C. Sänger, M. Schwentenwein, R. Bermejo, et al., "Hybridizing Lithography-Based Ceramic Additive Manufacturing With Two-Photon-Polymerization," *Applied Sciences* 13, no. 6 (2023): 3974, https://doi.org/10.3390/app13063974.

14. E. Balčiūnas, S. J. Baldock, N. Dreižė, et al., "3D Printing Hybrid Organometallic Polymer-Based Biomaterials via Laser Two-Photon Polymerization," *Polymer International* 68, no. 11 (2019): 1928–1940, https://doi.org/10.1002/pi.5909.

15. M. S. Saveleva, K. Eftekhari, A. Abalymov, et al., "Hierarchy of Hybrid Materials—The Place of Inorganics-in-Organics in it, Their Composition and Applications," *Frontiers in Chemistry* 7 (2019): 179, https://doi.org/10.3389/fchem.2019.00179.

16. N. I. Kilic, G. M. Saladino, S. Johansson, et al., "Two-Photon Polymerization Printing with High Metal Nanoparticle Loading," *ACS Applied Materials & Interfaces* 15 (2023): 49794–49804, https://doi.org/10.1021/acsami.3c10581.

17. E. Blasco, J. Müller, P. Müller, et al., "Fabrication of Conductive 3D Gold-Containing Microstructures via Direct Laser Writing," *Advanced Materials* 28 (2016): 3592–3595, https://doi.org/10.1002/adma.201506126.

18. S. K. Saha, B. Au, and J. S. Oakdale, "High-Speed Direct Laser Writing of Silver Nanostructures via Two-Photon Reduction," *Advanced Engineering Materials* 21, no. 9 (2019): 1900583, https://doi.org/10.1002/adem.201900583.

19. L. Yang, A. Rahimzadegan, V. Hahn, E. Blasco, C. Rockstuhl, and M. Wegener, "In Situ Diagnostics and Role of Light-Induced Forces in Metal Laser Nanoprinting," *Laser & Photonics Reviews* 16, no. 3 (2022): 2100411, https://doi.org/10.1002/lpor.202100411.

20. L. D. Zarzar, B. S. Swartzentruber, J. C. Harper, et al., "Multiphoton Lithography of Nanocrystalline Platinum and Palladium for Site-Specific Catalysis in 3D Microenvironments," *Journal of the American Chemical Society* 134 (2012): 4007–4010, https://doi.org/10.1021/ja211602t.

21. Y. Wang, C. Yi, W. Tian, F. Liu, and G. J. Cheng, "Free-Space Direct Nanoscale 3D Printing of Metals and Alloys Enabled by Two-Photon Decomposition and Ultrafast Optical Trapping," *Nature Materials* 23 (2024): 1645–1653, https://doi.org/10.1038/s41563-024-01984-z.

22. F. Li, S.-F. Liu, W. Liu, et al., "3D printing of Inorganic Nanomaterials by Photochemically Bonding Colloidal Nanocrystals," *Science* 381 (2023): 1468–1474, https://doi.org/10.1126/science.adg6681.

23. J. Kwon, H. Cho, Y. D. Suh, et al., "Flexible and Transparent Cu Electronics by Low-Temperature Acid-Assisted Laser Processing of Cu Nanoparticles," *Advanced Materials Technologies* 2 (2017): 1600222, https://doi.org/10.1002/admt.201600222.

24. S. H. Ko, H. Pan, C. P. Grigoropoulos, C. K. Luscombe, J. M. J. Fréchet, and D. Poulikakos, "All-inkjet-printed Flexible Electronics Fabrication on a Polymer Substrate by Low-temperature High-resolution Selective Laser Sintering of Metal Nanoparticles," *Nanotechnology* 18 (2007): 345202, https://doi.org/10.1088/0957-4484/18/34/345202.

25. C. Podder, X. Gong, X. Yu, W. Shou, and H. Pan, "Submicron Metal 3D Printing by Ultrafast Laser Heating and Induced Ligand Transformation of Nanocrystals," *ACS Applied Materials & Interfaces* 13 (2021): 42154–42163, https://doi.org/10.1021/acsami.1c10775.

26. M. Mukai, T. Kobayashi, M. Sato, et al., "Bubble Printing of Liquid Metal Colloidal Particles for Conductive Patterns," *Nanomaterials* 14 (2024): 1665, https://doi.org/10.3390/nano14201665.

27. E. Edri, N. Armon, E. Greenberg, et al., "Laser Printing of Multilayered Alternately Conducting and Insulating Microstructures," *ACS Applied Materials & Interfaces* 13 (2021): 36416–36425, https://doi.org/10.1021/acsami.1c06204.

28. E. Greenberg, N. Armon, O. Kapon, M. Ben-Ishai, and H. Shpaisman, "Nanostructure and Mechanism of Metal Deposition by a Laser-Induced Photothermal Reaction," *Advanced Materials Interfaces* 6, no. 14 (2019): 1900541, https://doi.org/10.1002/admi.201900541.

29. J. Bauer, C. Crook, A. Guell Izard, et al., "Additive Manufacturing of Ductile, Ultrastrong Polymer-Derived Nanoceramics," *Matter* 1 (2019): 1547–1556, https://doi.org/10.1016/j.matt.2019.09.009.

30. B. Cardenas-Benitez, C. Eschenbaum, D. Mager, et al., "Pyrolysis-induced Shrinking of Three-dimensional Structures Fabricated by Two-Photon Polymerization: Experiment and Theoretical Model," *Microsystems & Nanoengineering* 5 (2019): 38, https://doi.org/10.1038/s41378-019-0079-9.

31. J. Bauer, C. Crook, and T. Baldacchini, "A Sinterless, Low-temperature Route to 3D Print Nanoscale Optical-Grade Glass," *Science* 380 (2023): 960–966, https://doi.org/10.1126/science.abq3037.

32. B. Wang, A. Arab, J. Xie, et al., "The Influence of Microstructure on the Flexural Properties of 3D Printed Zirconia Part via Digital Light Processing Technology," *Materials* 15, no. 4 (2022): 1602, https://doi.org/10.3390/ma15041602.

33. M. Steurer, P. Somers, K. Kraft, et al., "Photothermal Laser Printing of Sub-Micrometer Crystalline ZnO Structures," *Advanced Science* 12, no. 4 (2025): 2410771, https://doi.org/10.1002/advs.202410771.

34. L. D. Zarzar, B. S. Swartzentruber, B. F. Donovan, P. E. Hopkins, and B. Kaehr, "Using Laser-Induced Thermal Voxels to Pattern Diverse Materials at the Solid–Liquid Interface," *ACS Applied Materials & Interfaces* 8 (2016): 21134–21139, https://doi.org/10.1021/acsami.6b06625.

35. A. C. Castonguay, N. N. Nova, L. M. Dueñas, et al., "Direct Laser Synthesis and Patterning of High Entropy Oxides From Liquid Precursors," *Materials Research Express* 10 (2023): 115003, https://doi.org/10.1088/2053-1591/ad068a.

36. W. Li, Y. He, S. Yang, et al., "Solution-Based Laser-Induced Silver Nanowire Growth on Substrates Through Photothermal and Chemical Comodulation," *The Journal of Physical Chemistry Letters* 16, no. 24 (2025): 6098–6105, https://doi.org/10.1021/acs.jpclett.5c01309.

37. J. Yeo, S. Hong, G. Kim, et al., "Laser-Induced Hydrothermal Growth of Heterogeneous Metal-Oxide Nanowire on Flexible Substrate by Laser Absorption Layer Design," *ACS Nano* 9 (2015): 6059–6068, https://doi.org/10.1021/acsnano.5b01125.

38. J. B. Mueller, J. Fischer, Y. J. Mange, T. Nann, and M. Wegener, "In-Situ Local Temperature Measurement During Three-Dimensional Direct Laser Writing," *Applied Physics Letters* 103, no. 12 (2013): 123107, https://doi.org/10.1063/1.4821556.

39. N. Misra, L. Xu, M. S. Rogers, S. H. Ko, and C. P. Grigoropoulos, "Pulsed Laser Annealing of Semiconductor Structures for Functional Devices," *Physica Status Solidi C* 5 (2008): 3264–3270, https://doi.org/10.1002/pssc.200779506.

40. C. Grigoropoulos, M. Rogers, S. H. Ko, A. A. Golovin, and B. J. Matkowsky, "Explosive Crystallization in the Presence of Melting," *Physical Review B* 73, no. 18 (2006): 184125, https://doi.org/10.1103/PhysRevB.73.184125.

41. C. Shi, X. Wang, Q. Zheng, et al., "Thermoreflectance-Based Thermometry of Silicon Thin Films with Resonantly Enhanced Temperature Sensitivity," *Optics Express* 32, no. 1 (2024): 1003–1009, https://doi.org/10.1364/OE.511938.

42. B. Figueroa, R. Hu, S. G. Rayner, Y. Zheng, and D. Fu, "Real-Time Microscale Temperature Imaging by Stimulated Raman Scattering," *The Journal of Physical Chemistry Letters* 11 (2020): 7083–7089, https://doi.org/10.1021/acs.jpclett.0c02029.

43. K. Green, K. Huang, H. Pan, G. Han, and S. F. Lim, "Optical Temperature Sensing with Infrared Excited Upconversion Nanoparticles," *Frontiers in Chemistry* 6 (2018): 416, https://doi.org/10.3389/fchem.2018.00416.

44. J. B. Mueller, J. Fischer, Y. J. Mange, T. Nann, and M. Wegener, "In-Situ Local Temperature Measurement During Three-Dimensional Direct Laser Writing," *Applied Physics Letters* 103, no. 12 (2013): 123107, https://doi.org/10.1063/1.4821556.

45. N. Do, L. Klees, P. T. Leung, F. Tong, W. P. Leung, and A. C. Tam, "Temperature Dependence of Optical Constants for Amorphous Silicon," *Applied Physics Letters* 60 (1992): 2186–2188, https://doi.org/10.1063/1.107074.

46. S. R. German, M. A. Edwards, Q. Chen, and H. S. White, "Laplace Pressure of Individual H_2 Nanobubbles From Pressure–Addition Electrochemistry," *Nano Letters* 16 (2016): 6691–6694, https://doi.org/10.1021/acs.nanolett.6b03590.

47. G. S. Manning, "On the Thermodynamic Stability of Bubbles, Immiscible Droplets, and Cavities," *Physical Chemistry Chemical Physics* 22 (2020): 17523–17531, https://doi.org/10.1039/D0CP02517H.

48. L. Makkonen and T. C. Vehmas, "On the Thermodynamic Stability of Bubbles, Immiscible Droplets, and Cavities by G. S. Manning, Phys. Chem. Chem. Phys., 2020, 22, 17523," *Physical Chemistry Chemical Physics* 23, no. 21 (2021): 12490–12492, https://doi.org/10.1039/D1CP01122G.

49. G. Cadilha Marques, L. Yang, Y. Liu, et al., "Fully Printed Electrolyte-Gated Transistor Formed in a 3D Polymer Reservoir with Laser Printed Drain/Source Electrodes," *Advanced Materials Technologies* 8, no. 22 (2023): 2300893, https://doi.org/10.1002/admt.202300893.

50. H. Lee, W. Manorotkul, J. Lee, et al., "Nanowire-on-Nanowire: All-Nanowire Electronics by on-Demand Selective Integration of Hierarchical Heterogeneous Nanowires," *ACS Nano* 11 (2017): 12311–12317, https://doi.org/10.1021/acsnano.7b06098.

51. N. Mohan, J. I. Ahuir-Torres, H. R. Kotadia, and G. Elger, "Laser Sintering of Cu Particle-Free Inks for High-Performance Printed Electronics," *npj Flexible Electronics* 9 (2025): 18, https://doi.org/10.1038/s41528-025-00389-5.

52. Z. Bai and J. Wei, "Focusing Error Detection Based on Astigmatic Method with a Double Cylindrical Lens Group," *Optics & Laser Technology* 106 (2018): 145–151, https://doi.org/10.1016/j.optlastec.2018.04.005.

53. F. Bachmann, R. Hielscher, and H. Schaeben, "Texture Analysis with MTEX—Free and Open Source Software Toolbox," *Solid State Phenomena* 160 (2010): 63–68, https://doi.org/10.4028/www.scientific.net/SSP.160.63.

Supporting Information

Additional supporting information can be found online in the Supporting Information section.

Supporting File 1: lpor71163-sup-0001-SuppMat.docx.

Supporting File 2: lpor71163-sup-0002-MovieS1.gif.